

Verification and validation of integrated simulation of energetic particles in fusion plasmas

S. Taimourzadeh¹, E.M. Bass², Y. Chen³, C. Collins⁴, N.N. Gorelenkov⁵, A. Könies⁶, Z.X. Lu^{7,8} , D.A. Spong⁹ , Y. Todo¹⁰ , M.E. Austin¹², J. Bao¹, A. Biancalani⁷, M. Borchardt⁶, A. Bottino⁷, W.W. Heidbrink¹ , R. Kleiber⁶, Z. Lin¹, A. Mishchenko⁷, L. Shi¹, J. Varela⁹, R.E. Waltz⁴ , G. Yu¹¹, W.L. Zhang^{1,13}  and Y. Zhu¹¹

¹ University of California, Irvine, CA, 92697, United States of America

² University of California San Diego, San Diego, CA 92093, United States of America

³ University of Colorado at Boulder, Boulder, CO 80309, United States of America

⁴ General Atomics, PO Box 85608, San Diego, CA 92186-5608, United States of America

⁵ Princeton Plasma Physics Laboratory, Princeton University, Princeton, NJ 08543, United States of America

⁶ Max Planck Institute for Plasma Physics, D-17491 Greifswald, Germany

⁷ Max Planck Institute for Plasma Physics, 85748 Garching, Germany

⁸ Fusion Simulation Center, Peking University, Beijing 100871, People's Republic of China

⁹ Oak Ridge National Laboratory, Oak Ridge, TN 37831, United States of America

¹⁰ National Institute for Fusion Science, Toki, Japan

¹¹ University of California, Davis, CA, 95616, United States of America

¹² University of Texas, Austin, TX, 78712, United States of America

¹³ Beijing National Laboratory for Condensed Matter Physics and CAS Key Laboratory of Soft Matter Physics, Institute of Physics, Chinese Academy of Sciences, Beijing 100190, China

E-mail: zhihongl@uci.edu

Received 19 November 2018, revised 18 February 2019

Accepted for publication 4 March 2019

Published 26 April 2019



CrossMark

Abstract

This paper reports verification and validation of linear simulations of Alfvén eigenmodes in the current ramp phase of DIII-D L-mode discharge #159243 using gyrokinetic, gyrokinetic-MHD hybrid, and eigenvalue codes. Using a classical fast ion profile, all simulation codes find that reversed shear Alfvén eigenmodes (RSAE) are the dominant instability. The real frequencies from all codes have a coefficient of variation of less than 5% for the most unstable modes with toroidal mode number $n = 4$ and 5. The simulated RSAE frequencies agree with experimental measurements if the minimum safety factor q_{\min} is adjusted, within experimental errors. The simulated growth rates exhibit greater variation, and simulations find that pressure gradients of thermal plasmas make a significant contribution to the growth rates. Mode structures of the dominant modes agree well among all codes. Moreover, using a calculated fast ion profile that takes into account the diffusion by multiple unstable modes, a toroidal Alfvén eigenmode (TAE) with $n = 6$ is found to be unstable in the outer edge, consistent with the experimental observations. Variations of the real frequencies and growth rates of the TAE are slightly larger than those of the RSAE. Finally, electron temperature fluctuations and radial phase shifts from simulations show no significant differences with the experimental data for the strong $n = 4$ RSAE, but significant differences for the weak $n = 6$ TAE. The verification and validation for the linear Alfvén eigenmodes is the first step to develop an integrated simulation of energetic particles confinement in burning plasmas incorporating multiple physical processes.

Keywords: RSAE, Alfvén eigenmodes, DIII-D tokamak, TAE, verification and validation, simulations, benchmark

(Some figures may appear in colour only in the online journal)

1. Introduction

Energetic particle (EP) confinement is a key physics issue for future burning plasma experiments, since ignition relies on self-heating by energetic fusion products (α -particles). EP transport can affect plasma profiles, beam deposition, and current drive, and can erode reactor walls [1]. Due to the strong coupling of EPs with burning thermal plasmas, plasma confinement properties in the ignition regime are some of the most uncertain factors when extrapolating from existing tokamaks to the international thermonuclear experimental reactor (ITER). Fully self-consistent simulations of EP transport and EP coupling with thermal plasmas must incorporate microturbulence and magnetohydrodynamic (MHD) instabilities with kinetic effects of both EPs and thermal plasmas on an equal footing, which requires an integrated kinetic-MHD simulation model based on the gyrokinetic formalism [2]. Coordinated efforts in verification and validation (V&V) are needed to develop integrated simulation tools for EP transport due to mesoscale Alfvénic instabilities primarily excited by EPs and EP coupling with microturbulence and macroscopic MHD modes mostly driven by thermal plasmas.

The first-principles simulations and reduced transport models are built upon a hierarchical construction of EP transport prediction based on more fundamental constituents by the progression from linear dispersion relation to nonlinear dynamics and eventually to EP transport. Nonlinear V&V will take on an increased importance as gyrokinetic and kinetic-MHD hybrid simulation models progress from linear to nonlinear simulations for understanding EP confinement properties regarding instability saturation mechanisms, interactions between mesoscale EP turbulence with microturbulence and MHD modes, and EP transport statistics. While it is unlikely that different models will agree in all situations, the regimes of deviation will need to at least be characterized and understood. This is a continuous process since models and computational methods evolve in time. As updated results become available from the first-principles models, they will provide new calibration points for the reduced EP transport models and stimulate their further development.

The V&V studies should use a hierarchical approach, starting with test cases from existing experiments and quantities that are well-diagnosed. For this purpose, an NBI-heated low-confinement (L-mode) plasma (DIII-D discharge #159243) with many small-amplitude RSAEs and toroidal Alfvén eigenmodes (TAEs), significant flattening of the EP profile, and strong microturbulence [3, 4] has been selected as the reference case for V&V studies by the Integrated Simulation of Energetic Particle (ISEP) project, part of the Scientific Discovery through Advanced Computing (SciDAC) initiative. High quality data for the AE structure, frequency,

and amplitude as well as the EP distribution, phase-space flows, and intermittent losses are all available from comprehensive DIII-D diagnostics. Taking advantage of this recent experimental progress, the early linear V&V studies [5] have been extended to nonlinear V&V studies of EP transport by using more newly available EP simulation codes and new EP reduced transport models. Linear and nonlinear simulations of AE and microturbulence in this reference case have been carried out by gyrokinetic, kinetic-MHD hybrid, and eigenvalue codes. Modeling of EP transport have also been carried out by reduced transport models. These V&V studies will proceed from linear simulation of instabilities, to nonlinear simulation of saturation mechanisms, to coupling of mesoscale turbulence with microturbulence and MHD modes, and finally to reduced EP transport models. The V&V for the linear simulations of Alfvén eigenmodes reported in this paper is the first step to develop an integrated simulation of energetic particles confinement in burning plasmas.

In this paper, we present linear simulations of RSAEs and TAEs observed in shot #159243 by using five initial value gyrokinetic codes (EUTERPE [6], GEM [7], GTC, GYRO, ORB5 [8]), two initial value gyrokinetic-MHD codes (FAR3D [9], MEGA [10]), and a perturbative eigenvalue code (NOVA-K [11]). Since fast ion profiles have the biggest uncertainty among all equilibrium profiles measured in the experiment, we use the fast ion profiles both from the kinetic EFIT reconstruction [12], which subtracts the thermal from the total plasma pressure, and from the more realistic kick model [13], which takes into account EP transport by the RSAEs and TAEs. The energetic particle distribution function, which is expected to be an anisotropic slowing-down in the experiment, is approximated by a Maxwellian in this V&V for all simulation codes. This approximation may cause some differences between simulations and experiments regarding the AE dispersion relation, especially the growth rate.

Using the EFIT fast ion profile, all simulation codes find that a RSAE is the dominant instability. The real frequencies from all eight codes have a coefficient of variation (CV) less than 5% for the most unstable modes with toroidal mode number $n = 4$ and 5. The simulated growth rates of these two RSAE exhibit greater variations with a CV up to 17% for the five gyrokinetic codes, and a CV up to 26% for all eight codes. Mode structures of the dominant modes agree well among all seven non-perturbative codes regarding radial eigenmodes, 2D shape on poloidal plane, ballooning characteristics, radial extent, and radial symmetry breaking. The TAE observed in the outer edge of the DIII-D experiment is not found in these initial value simulations using the EFIT fast ion profile, indicating that TAE is either linearly stable or sub-dominant to the RSAE. Using the outward-shifted fast ion profile from the kick model, GTC simulations find

the $n = 6$ TAE to be the dominant instability in the outer edge, consistent with the ECE data. Variations of the real frequencies and growth rates for this TAE from seven simulation codes are slightly larger than those of the RSAE, partially due to the co-existence of multiple radial eigenmodes with similar frequencies and growth rates. Finally, GTC simulation data, which has been processed by the Synthetic Diagnostic Platform (SDP) [14] to produce electron temperature fluctuations and radial phase shifts, is compared to the corresponding $n = 4$ and 6 ECE data for the experimental time of interest. The comparisons show no significant differences in radial mode structure for the strong $n = 4$ RSAE, but significant differences for the weak $n = 6$ TAE. These linear results provide a necessary foundation for the next step of nonlinear V&V studies.

The rest of the paper is organized as follows. In section 2, we describe the RSAE and TAE observations in the DIII-D experiment, and the equilibrium and profiles of this experiment as used in all simulation codes. In section 3, we compare different physics models and numerical parameters used in this V&V by all simulation codes. In section 4, we quantify the agreements and differences in RSAE and TAE linear dispersion from these eight independently developed simulation codes. In section 5, we process GTC data by a synthetic diagnostic to compare simulation results with the experimental ECE and ECEI data. Conclusions and discussions are presented in section 6.

2. DIII-D EP experiment for verification and validation

This work uses profiles and magnetic equilibrium obtained from DIII-D shot #159243 during L-mode current ramp phase at $t = 805$ ms, which has a safety factor, q , with reversed shear and $q_{\min} = 2.9$. Multiple unstable RSAEs and TAEs are excited using early deuterium beam power injected at 70–81 keV, with 4.0 MW of co-current, on-axis NBI, 0.7 MW of co-current, off-axis NBI, and 1.7 MW of counter-current, on-axis NBI. This discharge has excellent diagnostic coverage and was examined extensively in studies [3, 4, 15] of AE-induced fast-ion transport in critical gradient experiments.

Figure 1(a) shows the spectrogram of electron cyclotron emission (ECE) data during the current ramp for shot #159243, along with calculated RSAE frequency evolution from an ad hoc model [16]. The model was used to aid in toroidal mode number identification and to constrain the value of q_{\min} for the kinetic EFIT equilibrium reconstruction. In the zero-pressure limit, the RSAE frequency is $f_{\text{RSAE}} = (m - nq_{\min})V_A / (2\pi q_{\min}R)$, where V_A is the Alfvén speed and R is the major radius. The sensitive dependence on q_{\min} causes the RSAEs to chirp up in frequency over 20–40 ms as the q -profile evolves. The observed modes are also Doppler shifted due to toroidal rotation, with $f_{\text{lab}} = f + n f_{\text{rot}}$, where f_{rot} is the toroidal rotation frequency. In figure 1(a), RSAEs with multiple toroidal mode numbers appear simultaneously at the integer value $q_{\min} = 3$ near $t = 770$ ms. The relatively constant frequency modes are TAE modes. The approximate

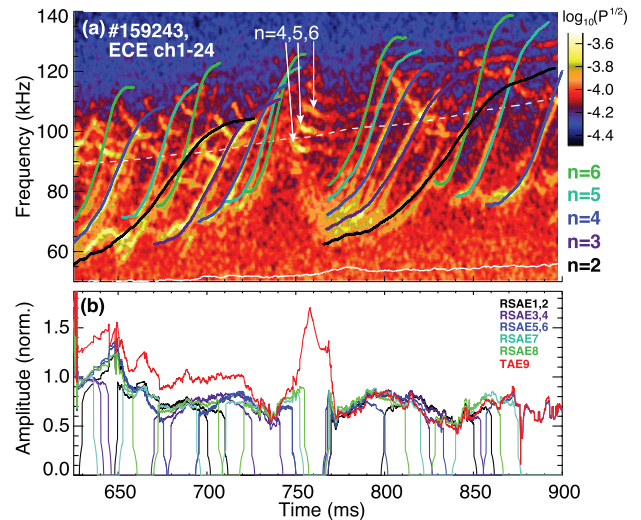


Figure 1. Reproduced courtesy of IAEA. Figure adapted from [15]. Copyright 2017 IAEA. (a) ECE power spectrum with RSAE time evolution fits from an ad hoc model [16] and calculated f_{GAM} (solid white line) and f_{TAE} frequencies (dashed white line, in plasma frame). (b) Time evolution of amplitudes determined from the kick model for DIII-D shot # 159243.

TAE frequency near q_{\min} is plotted as a dashed line, given by $f_{\text{TAE}} = V_A / (4\pi q_{\min}R)$.

2.1. Experiment fast-ion profile

While diagnostics provide measurements of portions of the fast-ion distribution, we are unfortunately not able to reconstruct the entire experimental fast-ion distribution function. Instead, an estimate of the experimental fast-ion pressure profile is obtained by subtracting the measured thermal pressure from the computed total pressure from the kinetic EFIT equilibrium reconstruction, which is constrained by Motional Stark Effect measurements, external magnetics data, and knowledge of q_{\min} from AE behavior. The kinetic EFIT fast ion density profile is shown in figure 2.

As described in [15], a more realistic fast-ion pressure profile was obtained using the time-dependent kick model of AE transport [17]. The kick model computes the probability for AE-induced change in energy and toroidal angular momentum throughout fast-ion phase space and evolves the fast-ion distribution function through the TRANSP-NUBEAM code. In this case, AE mode structures were first computed by the NOVA code and then scaled to match experiment measurements at a single timeslice. The kick model then evolved the mode amplitudes in time (figure 1(b)) so that the modeled neutron rate matched the measured value. The resulting fast-ion profile agrees well with experimental measurements [4]. The kick model fast ion pressure profile is used in section 4.2.

2.2. Equilibrium and profile comparison

All benchmarking codes use magnetic equilibria calculated from EFIT [18], except for FAR3D and EUTERPE which use the same equilibrium calculated from VMEC [19]. Profiles are

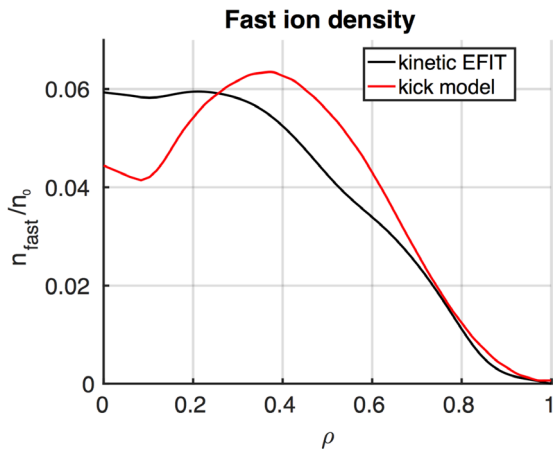


Figure 2. DIII-D shot 159243.00805 fast ion density calculation comparison of kinetic EFIT versus the kick model. On-axis electron density $n_0 = 3.29 \times 10^{13} \text{ cm}^{-3}$.

obtained using kinetic EFIT calculations. Figure 3 shows the equilibrium and profiles for all codes, as outputted from each code, after the experimental inputs have been internally processed. Note, while this may seem trivial, with a verification exercise of this magnitude it is an absolutely essential first step. Figure 3(a) depicts ten magnetic flux surfaces ranging from $\rho = 0.1$ –1.0 in uniform steps, where ρ is the square root of the toroidal flux normalized by its separatrix value. Figure 3(b) shows the magnetic field magnitude on the low and high field sides of the mid-plane, respectively. Magnetic surfaces align within tolerance and magnetic field magnitudes are almost identical with the exception that it, on the low field side at $\rho = 1.0$, is 3% larger in NOVA. Figures 3(c) and (d) show that the q profile, density profiles, and temperature profiles are almost identical for all codes.

3. Simulation models

This paper presents linear AE simulations of the DIII-D EP experiment described in section 2 by using a perturbative eigenvalue code (NOVA-K), and seven non-perturbative initial value codes including five gyrokinetic codes (EUTERPE, GEM, GTC, GYRO, ORB5) and two gyrokinetic-MHD hybrid codes (FAR3D, MEGA). A tabulated comparison summary of the different codes is presented in table 1. Detailed comparisons of all codes can be found in appendix.

4. Simulation results

4.1. RSAE

Using the equilibrium and profiles from figure 3, linear electromagnetic simulations from all codes find an unstable RSAE, peaked at the $q_{\min} = 2.94$ surface, to be the dominant linear instability for DIII-D shot #159243 at 805 ms. The RSAE linear dispersion has been obtained and is presented in figure 4. In the figure, codes are grouped according to physics model via the plot marker used. Namely, diamond, star, and

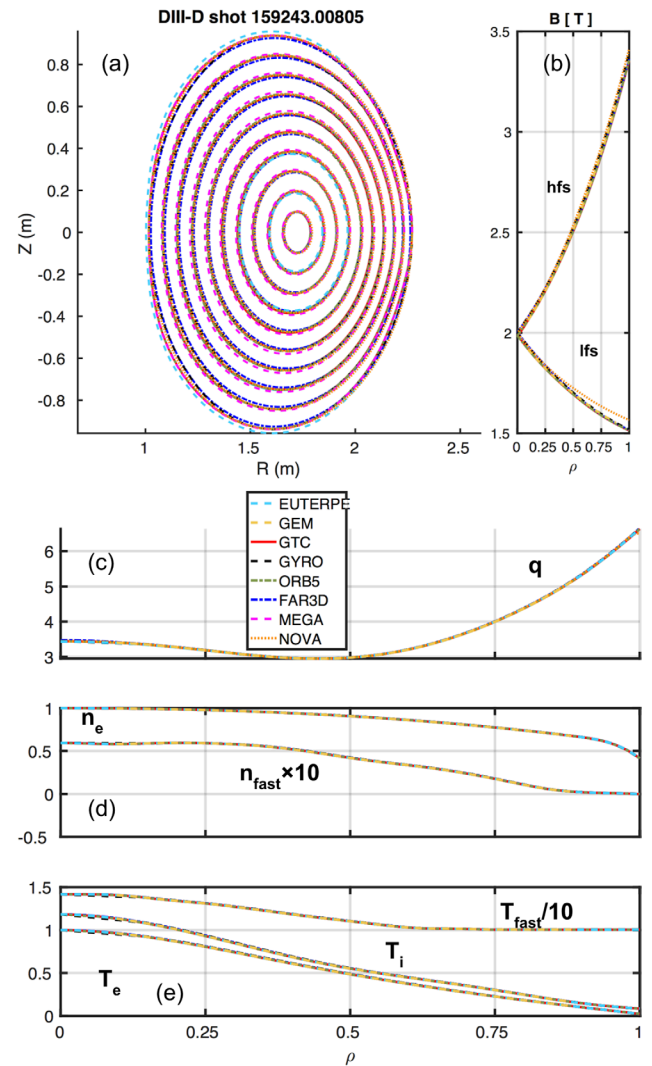


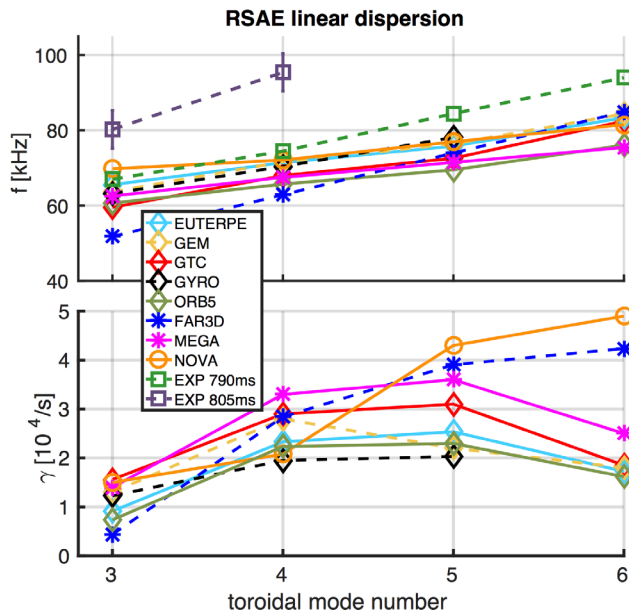
Figure 3. Equilibrium geometry and profiles, for DIII-D shot 158243 at 805 ms, outputted from all benchmarking codes, after experimental inputs have been processed. (a) Ten magnetic flux surfaces ranging from $\rho = 0.1$ –1.0. (b) Magnetic field amplitude on the mid-plane for the high field side and low field side. (c) q profile with $q_{\min} = 2.94$. (d) Electron and fast ion densities normalized to the electron on axis value ($n_0 = 3.29 \times 10^{13} \text{ cm}^{-3}$). (e) Electron, thermal ion, and fast ion temperatures normalized to the electron on-axis value ($T_{e,0} = 1689 \text{ eV}$).

circle markers are used for the gyrokinetic, gyrokinetic-MHD hybrid, and perturbative eigenvalue codes, respectively.

All models show excellent agreement in real frequency. The coefficients of variation of real frequency values, $CV_\omega = \sigma_\omega / \mu_\omega$, where σ and μ are the standard deviation and mean, respectively, for all data points per toroidal mode number in the dispersion are presented in table 2, which shows that $CV_\omega < 5\%$ throughout the dispersion, with the exception of the subdominant toroidal mode, $n = 3$, where $CV_\omega = 8.4\%$. Figure 4 also contains ECE measured frequency values, which are shifted into the plasma frame, and are grouped with square plot markers. The ECE values are plotted for two experimental times in the discharge, 790 ms and 805 ms, to give a qualitative estimation of rate of change of the experimental q_{\min} value.

Table 1. Comparison of simulation models used in this benchmark.

| Code | Electrons | Ions | Fast ions | δB_{\parallel} | type |
|---------|--|--|--------------------|------------------------|---------------|
| EUTERPE | PIC DK | PIC GK | PIC GK | No | Initial value |
| GEM | PIC DK | PIC GK | PIC GK | No | Initial value |
| GTC | Fluid-kinetic hybrid | PIC GK | PIC GK | No | Initial value |
| GYRO | Continuum DK | Continuum GK | Continuum GK | No | Initial value |
| ORB5 | PIC DK | PIC GK | PIC GK | No | Initial value |
| FAR3D | Fluid + perturbative Landau damping | Fluid + perturbative Landau damping | Gyrofluid closures | No | Eigenvalue |
| MEGA | Fluid | Fluid | PIC GK | Yes | Initial value |
| NOVA | Fluid | Fluid | Kinetic | Yes | Eigenvalue |

**Figure 4.** Linear dispersion relation calculation for RSAE in DIII-D shot 158243 at 805 ms. (a) Real frequencies. (b) Growth rates. The plot markers are diamond, star, and circle for the gyrokinetic, kinetic-MHD hybrid, and perturbative eigenvalue codes, respectively.

Simulation results agree better with the ECE frequency value at 790ms, which is due to limitations in the accuracy of the q_{\min} calculation in the equilibrium reconstruction. For context, errors as small as 1% in q_{\min} can lead to variations in frequency as high as 18%. q_{\min} can be manually changed until simulation frequency values agree with the ECE data at 805ms, but here we accept the EFIT calculations as they are.

Growth rates exhibit greater variations than those in the real frequency comparison. Nonetheless, there is agreement in the general trend of the dispersion, with $n = 4$ or 5 being the dominant mode. FAR3D and NOVA show exceptions to this trend, as the growth rates are found to increase monotonically. For NOVA, this is expected as some damping mechanisms are ignored, such as the radiative damping for RSAEs which is expected to increase strongly with the toroidal mode number. For TAE modes the radiative damping is added via the analytic expression developed earlier [20]. FAR3D uses Padé approximate fits to the Bessel functions entering into the fast ion moment equations for the energetic particle FLR effects and a first order expansion for the thermal ion FLR

Table 2. Real frequency coefficients of variation.

| | $n = 3$ | $n = 4$ | $n = 5$ | $n = 6$ |
|---------------|---------|---------|---------|---------|
| CV_{ω} | 8.4% | 4.8% | 4.0% | 4.8% |

effects (in the vorticity equation). Taking into account the perpendicular wave numbers that can be inferred from the dominant components in the calculated mode structures, and the fast and thermal ion energies, these approximations have been checked and should be valid. However, as indicated in figure 4(b), there are deviations in the FAR3D growth rates from the gyrokinetic results particularly at $n = 6$, and, to a lesser degree at $n = 5$. This may be due to the subdominant modes having stronger spatial variations that create effective wave-numbers somewhat beyond the range of the FLR approximations. Moreover, the fast-ion gyro-fluid model used in FAR3D uses two moment equation, yet more may be needed. Also, the $n = 6$ data for GYRO is not presented here, as a coexistent ITG mode was observed to affect the numerical properties of the simulation. The coefficient of variation for $n = 4, 5$ is $CV_{\gamma} = 16\%, 17\%$, for the gyrokinetic codes, and $CV_{\gamma} = 18\%, 26\%$ for all codes.

Even with physics model differences, mode structures agree well between all codes. Figure 5 shows the radial structures of the poloidally-rms-averaged dominant poloidal harmonic, and two accompanying side bands, for the $n = 4$ RSAE. All codes show maximum mode intensity localized near the q_{\min} surface, $\rho = 0.44$, with the FWHM mean value and the coefficient of variation of the dominant poloidal harmonic being $\Delta\rho_{\text{FWHM}} = 0.13$, and 0.12 , where ρ is the normalized square root of the toroidal flux, $CV_{\text{FWHM}} = 7.7\%$, and 15% for the gyrokinetic codes and all of the codes, respectively. The distance between the two $q = 3$ surfaces is comparable to RSAE radial mode width ($\Delta\rho \sim 0.16$) as shown in figure 5. Figure 6 shows the two dimensional RSAE eigenfunction structures, which show agreement in 2D shape on the poloidal plane, ballooning characteristics, radial extent and radial symmetry breaking. In the MHD limit the Alfvén mode structure is up-down symmetric; the presence of an EP component breaks this symmetry and leads to the teardrop/triangular shaped mode structures. These drift effects on TAE mode structures were first presented in figure 14 of [21]; and later discussed for RSAE modes in [5, 22, 23], and experimentally in figures 6 and 7 of [24]. The differences in linear mode structures are not significant and most likely not detectable in experiments since

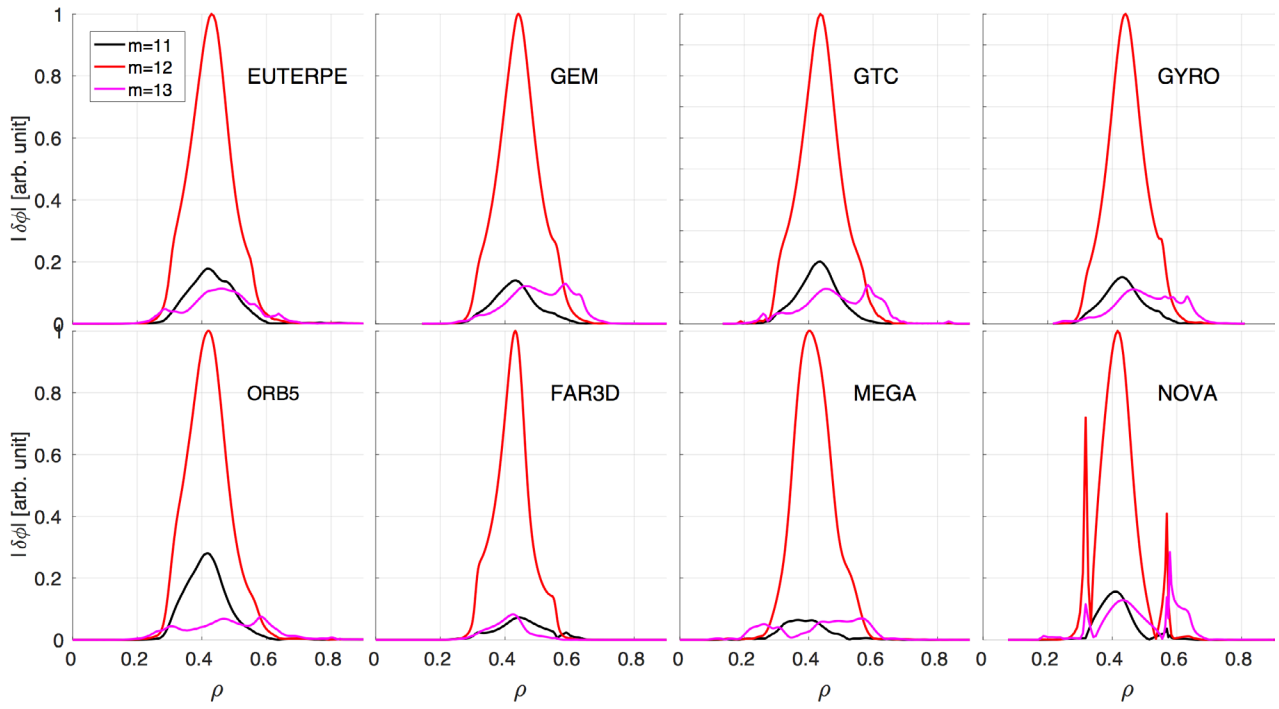


Figure 5. Poloidally-rms-averaged radial mode structures of the $n = 4$ RSAE's dominant poloidal harmonic and two side bands.

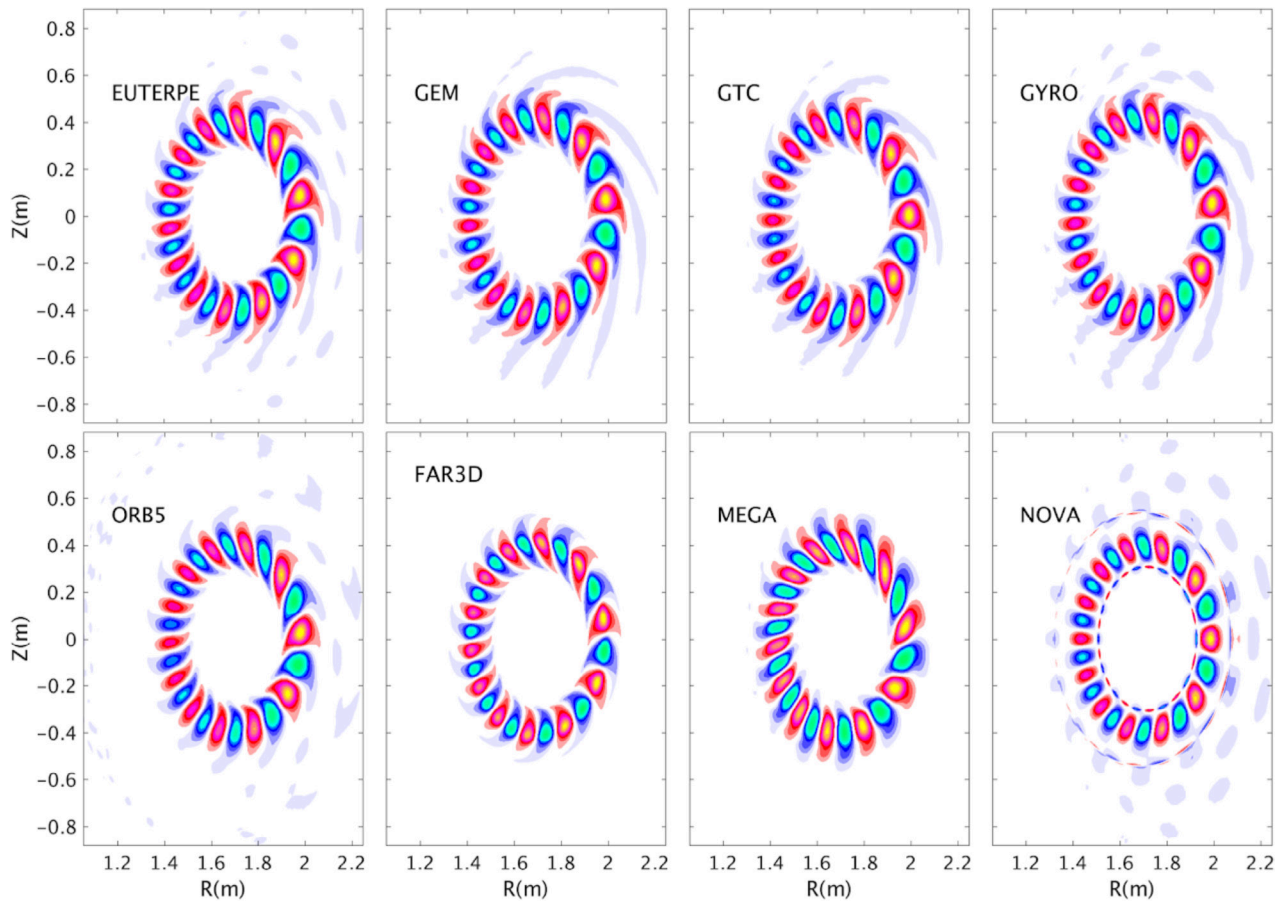


Figure 6. $n = 4$ poloidal cross section RSAE structures for DIII-D shot 158243 at 805 ms.

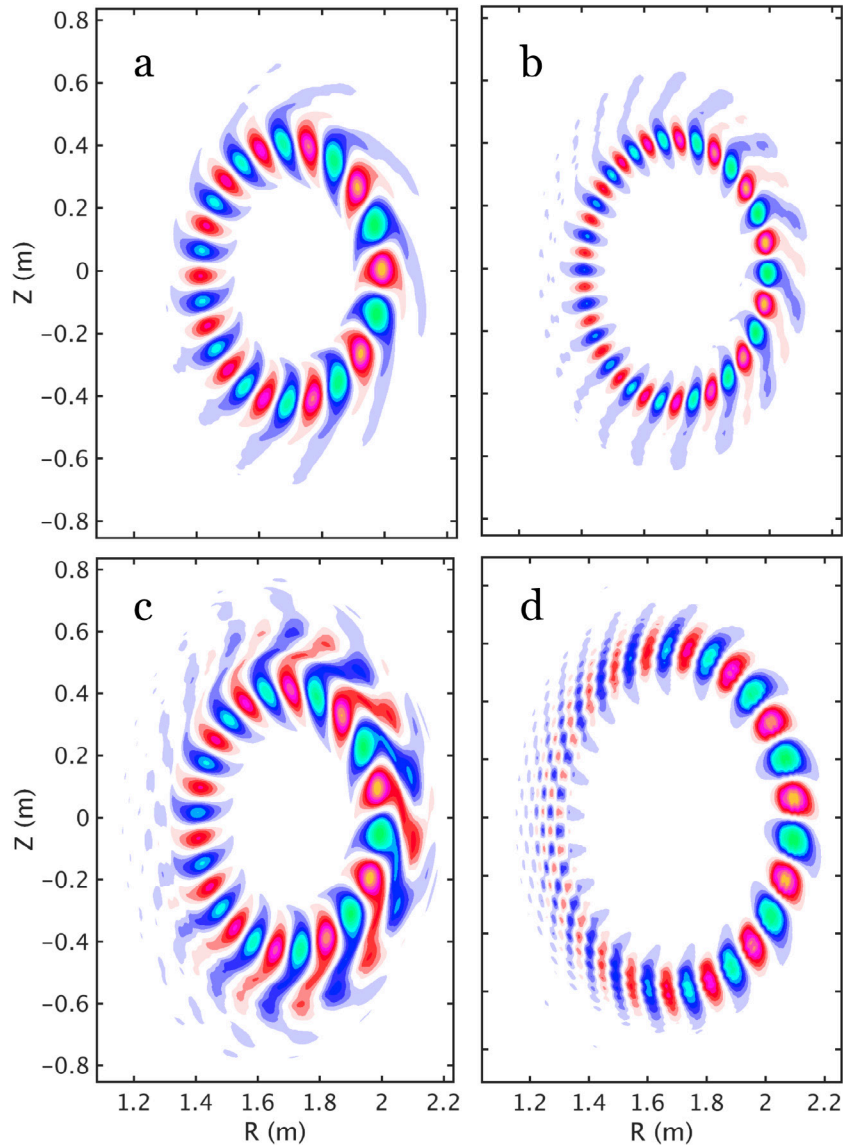


Figure 7. Perturbed electrostatic potential from GTC simulations of DIII-D shot 159243.00805. ((a)–(b)) $n = 4$ and $n = 6$ simulations, respectively, using a fast ion density profile calculated from kinetic EFIT. ((c)–(d)) $n = 4$ and $n = 6$ simulations, respectively, using a fast ion density profile calculated from the kick model.

other effects, such as nonlinear effects, could cause larger differences than those between codes.

Furthermore, the significance of the effects of thermal ion and electron gradients on the $n = 4$ RSAE instability drive has been examined by several codes, which found that there is a large thermal plasma contribution to the destabilization of the AEs in this case, consistent with theoretical expectations [25]. In the absence of any thermal plasma density or temperature gradients, GEM, GTC, and GYRO growth rates for the $n = 4$ RSAE are found to be reduced by 100%, 85%, and 62%, respectively.

4.2. TAE

In addition to RSAEs, experimental observations also find unstable TAEs at 805 ms, as shown in figure 1. Spatial analysis of the ECE data shows that the TAEs are localized near $\rho \approx 0.75$. To see if simulation can find an unstable TAE, the

radial domain is restricted to the range $\rho = [0.564–0.902]$ in a GTC simulation to avoid the dominant RSAE. In doing so, linear simulations do show a marginally unstable TAE with $\omega = 99$ kHz and $\gamma/\omega = 0.0121$. The approximation of energetic particle distribution as Maxwellian may cause some errors in the TAE growth rate. However, previous simulations in other work using an anisotropic slowing-down found only small differences in the TAE growth rate.

To see if a linearly unstable TAE appears without artificial domain restrictions, we use a more realistic fast-ion density profile taking into account transport caused by the AE, calculated from the kick model [17]. The kick model is used, as the actual fast-ion distribution is not able to be reconstructed from measurements. Figure 2 compares the fast-ion density profiles from the kinetic EFIT and the kick model. The figure shows that the kick model calculation predicts a higher density and larger gradients beyond $\rho = 0.4$ than the kinetic EFIT prediction. These two profiles are used in GTC $n = 4$ and $n = 6$

Table 3. $n = 6$ real frequencies (in the plasma frame) and growth rates for DIII-D 159293.00805 simulations using a fast-ion density profile calculated using the kick model, scaled upwards by a factor of 1.5 times, and the corresponding coefficient of variation of the results. ECE frequency data at 805 ms is also included.

| | EUTERPE | GEM | GTC | GYRO | ORB5 | FAR3D | NOVA | ECE (805 ms) |
|------------------------------------|---------|------|------|------|------|-------|------|--------------|
| f (kHz) | 100 | 102 | 95.2 | 79.2 | 95.2 | 97.7 | 92.6 | 98.9 |
| γ (10^3 s^{-1}) | 54.4 | 20.7 | 55.8 | 48.3 | 60.7 | 3.56 | 5.35 | |

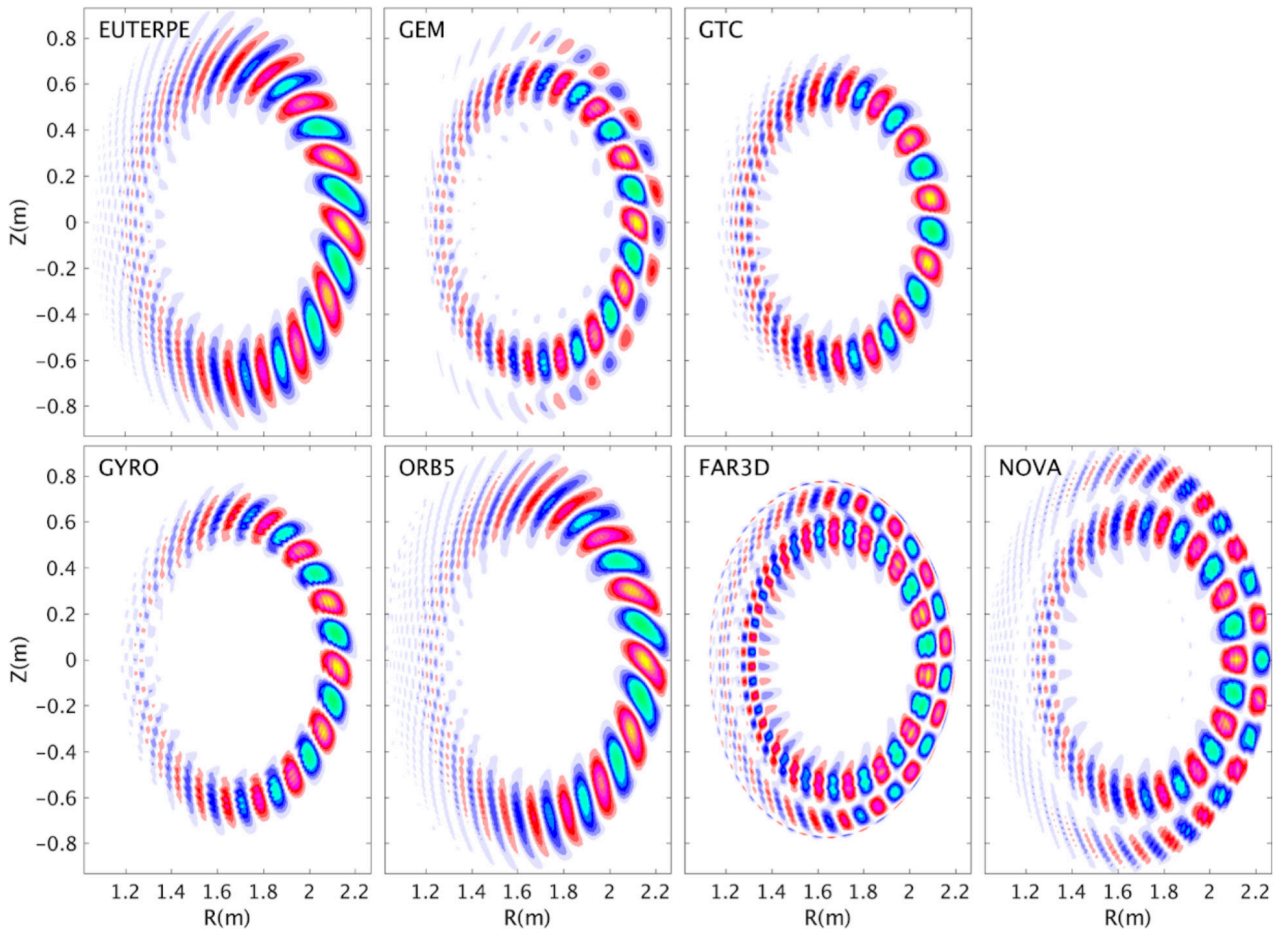


Figure 8. Poloidal cross section of the perturbed electric potential for the $n = 6$ TAE, using the kick model fast ion density profile, for DIII-D shot 158243 at 805 ms.

simulations, using all other equilibrium quantities as shown in figure 3. Figure 7 shows the obtained 2D modes structures of the perturbed electrostatic potential for these four simulations. The top row shows the $n = 4$ and 6 mode structures, both of which show an unstable RSAE, with no TAE, obtained using the kinetic EFIT profile. The bottom row shows a transition of the dominant mode from RSAE to TAE as the toroidal mode number increases from $n = 4$ to $n = 6$. From figure 7(c), it can be seen that the dominant $n = 4$ RSAE is accompanied by a lower amplitude TAE at larger radius. The real frequency for the $n = 4$ RSAE shows almost no difference if using the kinetic EFIT or kick model profiles, but the growth rate is 30% lower when using the kick model profile.

After observing the differences in the fast ion density profiles between the kinetic EFIT and kick model in GTC AE simulations, a verification test is carried out for the $n = 6$ TAE

mode, using the kick model fast ion density profile scaled upwards by a factor of 1.5 times. This increase of the fast-ion density is done so as to ensure that all codes yield unstable results. Table 3 tabulates the calculated TAE frequency and growth rates for $n = 6$, from seven codes, along with the measured ECE frequency (shifted into the plasma frame). The mean of the calculated real frequencies shows a 6.0% difference from the experimental ECE value, and variation between codes is characterized by $CV_\omega = 7.9\%$. Growth rates vary much more significantly, however, with $CV_\gamma = 33\%$ for the gyrokinetic codes. This discrepancy correlates with different observed mode structures between codes. Figure 8 shows the 2D mode structures for the perturbed electrostatic potentials in poloidal cross sections. Here, it can be seen that there are three patterns of structures, each with one, two, or three local peaks of mode amplitude. The radial eigenfunctions can be

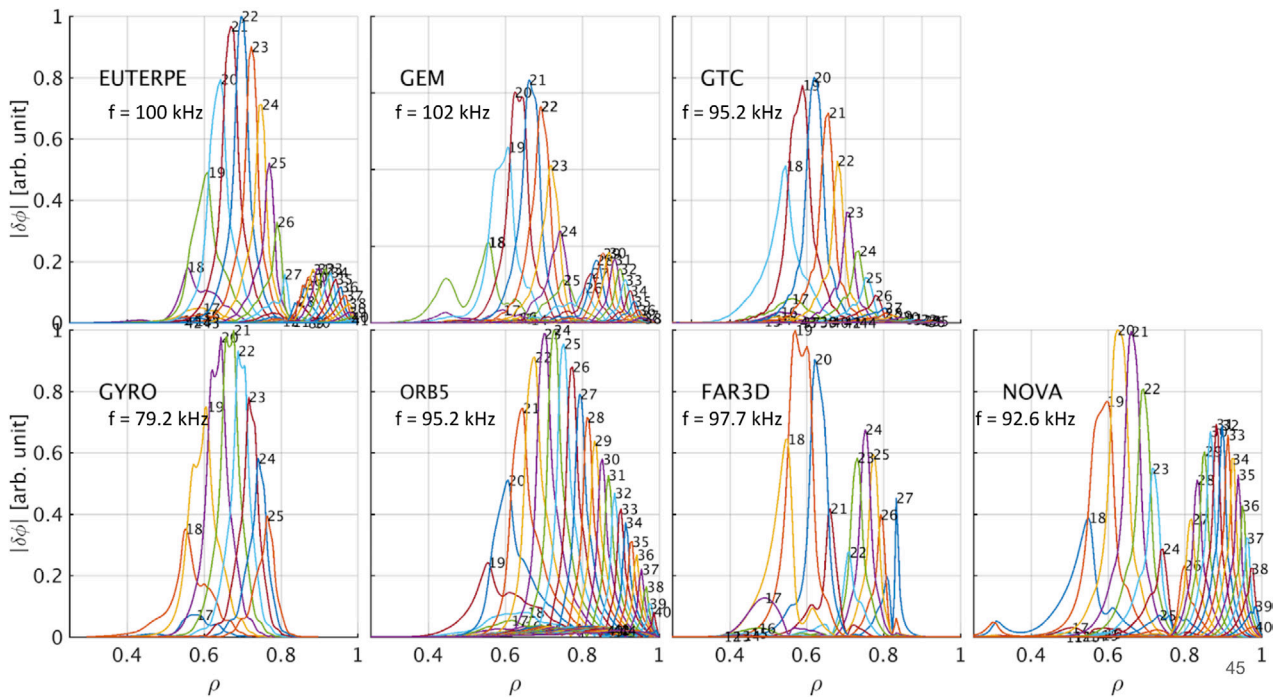


Figure 9. Radial structures of the poloidal harmonics of the electrostatic potential for the $n = 6$ TAE, using the kick model fast ion density profile, for DIII-D shot 158243 at 805 ms. The simulated TAE frequency for each code is written in each panel.

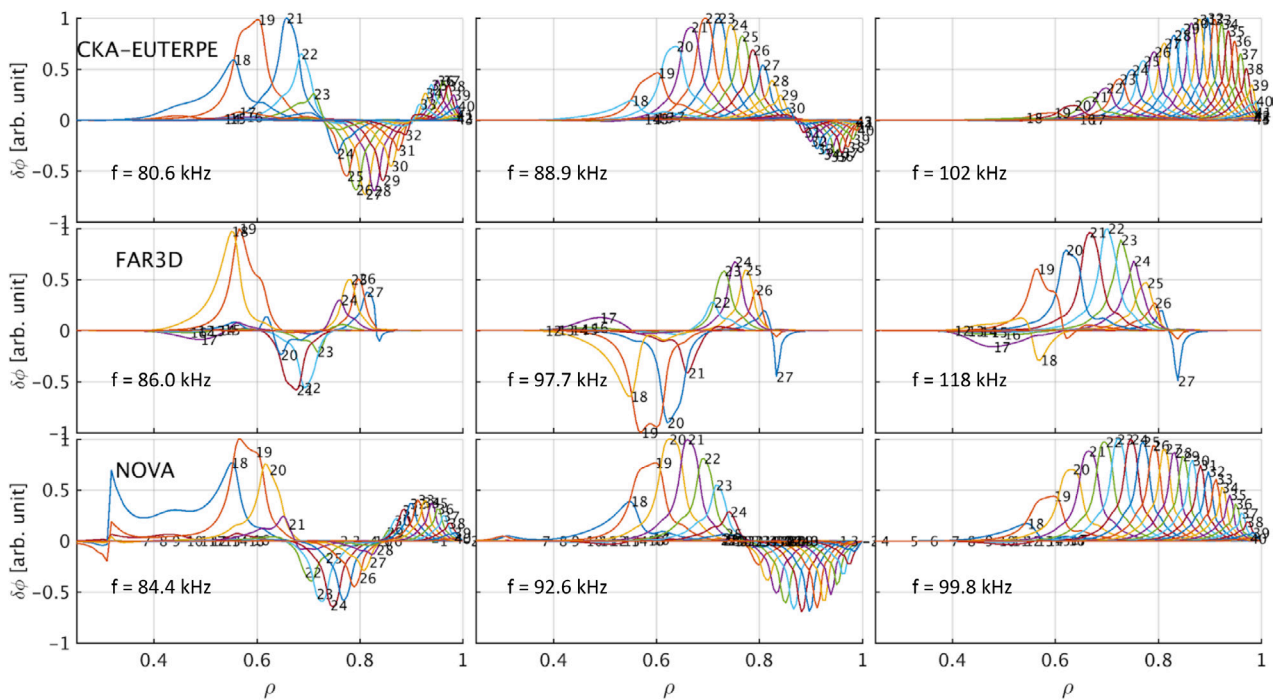


Figure 10. Radial TAE mode structures from TAE frequency scan using fast ion density calculated from the kick-model. (Top row) CKA-EUTERPE runs with $f = [80.6, 88.7, 102]$ kHz. (middle row) FAR3D eigenvalue runs with $f = [86.0, 97.7, 118]$ kHz. (bottom row) NOVA frequency scan with $f = [84.4, 92.6, 99.8]$ kHz. In the figure, frequencies increase from left to right.

seen in figure 9, which shows the corresponding three radial eigenstates with zero, one, and two crossings of the zero value for the electrostatic potential.

The discrepancy between the mode structures between codes is consistent with the discrepancy in the real frequency. This is seen in a frequency scan using NOVA simulations, FAR3D's eigenvalue solver and the CKA-EUTERPE code.

The scans reproduce the three mode structures of figure 9, and the radial structures of these three radial eigenstates are shown in figure 10. The bottom row shows the NOVA scan of frequency values $f = [84.4, 92.6, 99.8]$ kHz, the middle row shows FAR3D scan with $f = [86.0, 97.7, 118]$ kHz and the top row shows the CKA-EUTERPE results with $f = [80.6, 88.7, 102]$ kHz. The figure shows that the TAE

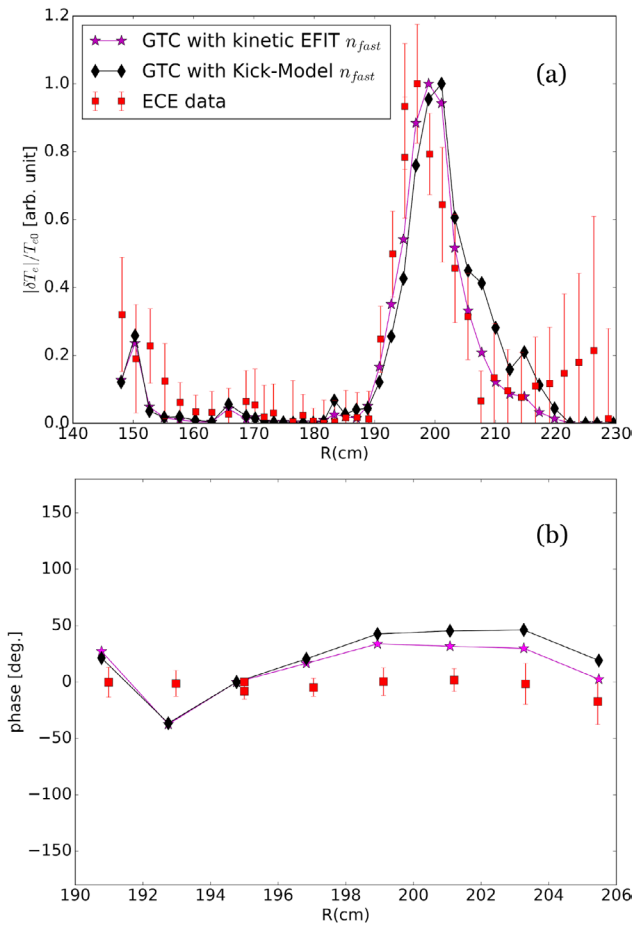


Figure 11. Comparison of GTC simulation data, after being processed through the synthetic-diagnostic-platform, to experimental ECE data for DIII-D #159243 at 805 ms. (a) Radial structure of $|\delta T_e|/T_{e0}$. (b) The phase profile relative to $R = 195.0$ cm.

solution space is frequency dependent, but the dependency is different between the different codes.

5. Comparison to experimental values

Experimental data from the DIII-D ECE radiometer [26] has been obtained for validation purposes. The data corresponds to the lowest radial harmonic of the $n = 4$ mode, which is averaged over 11 steps in the time range [791.5, 802.5] ms of the DIII-D shot #158243. Corresponding data for the $n = 6$ mode is also obtained. The diagnostic spans the frequency range [83.5, 129.5] GHz in 40 channels, providing diagnostic coverage in the radial range $R = [148.1, 228.7]$ cm, where R is the major radius, 4 cm above the midplane. We compare the measured and simulated radial structure of the magnitude of the mode amplitude, $|\delta T_e|/T_{e0}$, where δT_e and T_{e0} are the perturbed and equilibrium electron temperatures, respectively, and phase profile relative to a specified radial location.

For this comparison, GTC has been interfaced with the open source Synthetic Diagnostic Platform (SDP) [14], where GTC simulation data is processed through SDP. Figure 11(a) shows $|\delta T_e|/T_{e0}$, obtained from GTC via SDP, for both the kinetic EFIT (black) and kick model (magenta) fast-ion

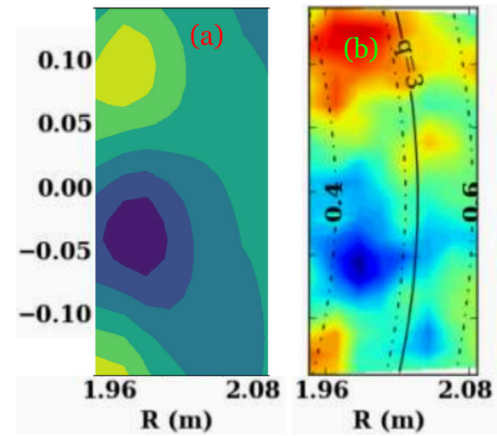


Figure 12. Comparison of $n = 4$ RSAE mode GTC simulation data and experimental ECEI data for DIII-D #159243 at 807.3 ms. 2D structure on a poloidal plane of $\delta T_e/T_{e0}$ for (a) GTC simulation data, after being processed through the synthetic-diagnostic-platform, and (b) experimental ECEI data.

density profiles and the experimental data (red). The GTC data corresponds to the two $n = 4$ RSAE-dominated cases in figures 7(a) and (c). All three structures show peak amplitude near $R \approx 198$ cm. The full width half max are nearly the same, with that from the kick-model being slightly larger. These results show there is no significant difference in $|\delta T_e|/T_{e0}$ of the RSAE between simulations and the experimental data, when using either the kinetic EFIT or kick model fast ion density profiles. The experimental data may indicate the presence of radially increasing fluctuations between $R = [210, 220]$ cm, which may correspond to TAE activity; however, the uncertainty in the data is large in that region. Figure 11(b) shows the mode's phase difference for different radial locations, relative to $R = 195.0$ cm, for the experimental data and the GTC simulations with the kinetic EFIT and kick model fast ion density profiles. The disagreement between the phase values for the GTC simulations with the kinetic EFIT and kick model fast ion density profiles in the outer radial regions is due to the presence of a subdominant TAE near $R \approx 215$ cm in the simulation using the kick model fast ion density.

The comparison of the $n = 4$ simulated RSAE has been extended to 2D ECEI data for the $n = 4$ mode of DIII-D shot #159243 at 807.3 ms. Figures 12(a) and (b) show GTC $n = 4$ RSAE data of δT_e , processed through SDP, and the $n = 4$ mode filtered ECEI data, respectively. The comparison shows that the simulated and experimental data agree well in mode location, radial extent, and shape. In both cases, the mode is peaked at the $q_{\min} = 2.94$ location.

Comparison of GTC $n = 6$ simulation data, via SDP, with experimental ECE data does show a significant difference between experimental data and GTC simulations using the kinetic EFIT or kick model fast-ion density calculations. Figure 13(a) shows the $|\delta T_e|/T_{e0}$ profiles for GTC simulation results and the experimental ECE data. The ECE data shows peak magnitude near $R \approx 226$ cm, and the peak amplitudes from GTC simulations are $R = 201.1$ cm and $R = 210.0$ cm for the kinetic EFIT and kick model results, respectively. Qualitatively, there is a better agreement of experimental data

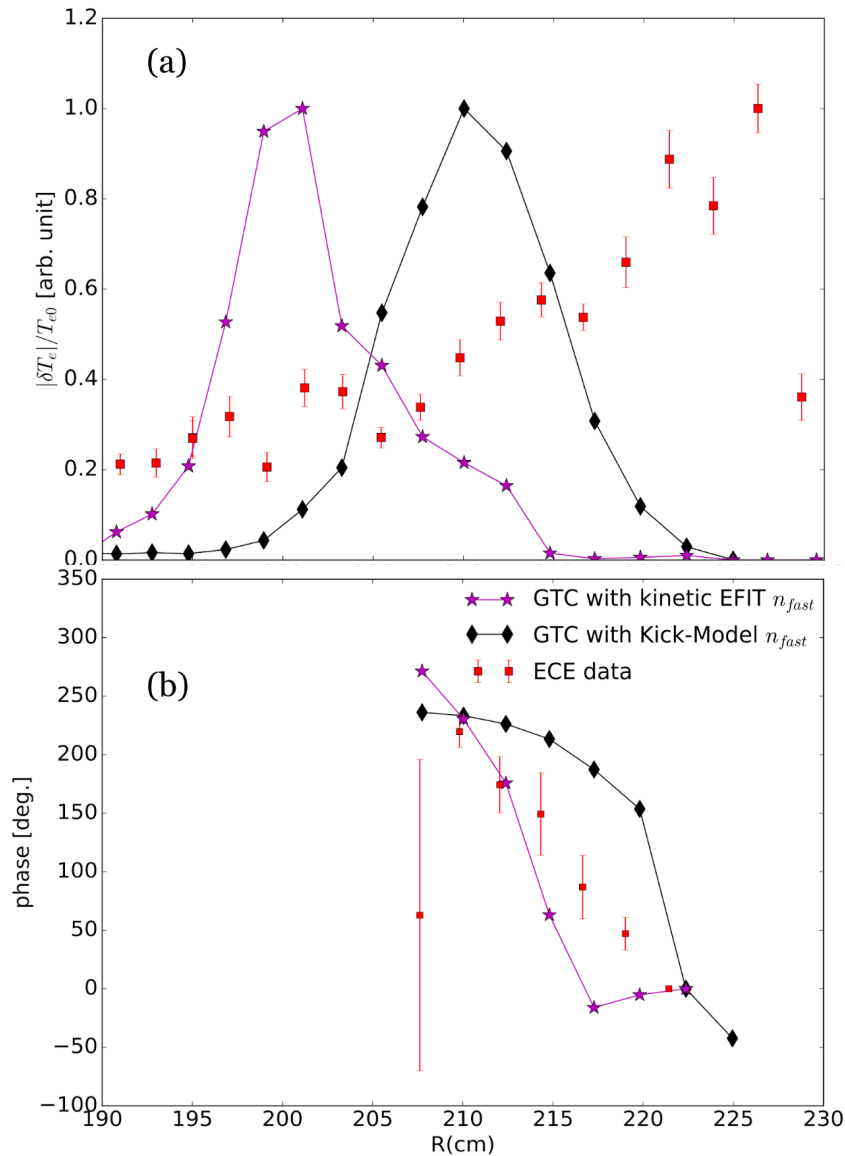


Figure 13. Comparison of GTC simulation data, after being processed through the synthetic-diagnostic-platform, to experimental ECE data for DIII-D #159243 at 805 ms. (a) Radial structure of $|\delta T_e|/T_{e0}$. (b) The phase profile relative to $R = 221.4$ cm. The measured $n = 6$ TAE ECE frequency is 98.9 kHz (plasma frame) and the GTC calculated value is 95.2 kHz.

with the kick model result than the kinetic EFIT simulation result. The large discrepancy in location of the peak magnitude between the kick model simulation result and experiment may be attributed to the kick model's prediction of the outward shift of the fast ion density profile gradients being too modest, but further testing is needed to confirm this. Another reason for the discrepancy may be that the experimentally observed TAE is simply nonlinearly generated, which cannot be reproduced in linear simulations. Figure 13(b) shows the mode's phase difference for different radial locations, relative to $R = 221.4$ cm, for the GTC results and the experiment, in the radial range $R = [195.0, 225.0]$ cm.

In both figures 11(b) and 13(b), there is a large difference between the simulation and experimental phase values, although the overall radial trends of the phases qualitatively agree. This may indicate that there are dominant nonlinear physics present in the experiment that cannot be reproduced in these linear simulations.

6. Conclusion and discussion

Using kinetic EFIT equilibrium data from DIII-D shot #159243, gyrokinetic, gyrokinetic-MHD hybrid, and perturbative eigenvalue simulations have obtained the RSAE linear dispersion of toroidal mode numbers $n = [3, 6]$, for verification and validation purposes. The simulations are conducted using five initial value gyrokinetic codes (EUTERPE, GEM, GTC, GYRO, ORB5), two initial value kinetic-MHD codes (FAR3D, MEGA), and a perturbative eigenvalue code (NOVA-K). All simulation results predict a linearly unstable RSAE and find excellent agreement in mode structure and real frequency. Simulated RSAE frequencies agree well with experimental ECE values for the experimental time of 790 ms, rather than 805 ms from which time profiles are taken. This discrepancy between simulation results and experimental data is due to small error in the reconstructed equilibrium q_{min} value. Growth rates are found to show a larger variance,

with a coefficient of variation of 18% for the dominant mode number.

Moreover, experimental measurements observe the presence of TAE modes in the outer edge. Therefore linear simulations are repeated with a more realistic fast ion density profile obtained using the kick model, which takes AE induced transport into account. Using this fast ion profile, GTC simulations show that the observed instability transitions from RSAE to TAE as the toroidal mode number is increased from $n = 4$ to $n = 6$, whereas no TAE is observed when using the EFIT fast ion profile. TAE simulations from seven codes find variations of the real frequencies and growth rates are slightly larger than those of the RSAE, partially due to the co-existence of multiple radial eigenmodes with similar frequencies and growth rates.

Further validations are obtained by comparing GTC simulation data, processed through the synthetic-diagnostic-platform, for $n = 4$ and $n = 6$, using both the kinetic EFIT and kick model predicted fast ion density profiles, to experimental ECE measurements of $|\delta T_e|/T_{e0}$ and phase profiles. The comparisons shows excellent agreement in radial mode structure of $n = 4$, for both fast ion density profiles. The $n = 4$ comparison is also extended to ECEI data, where agreement is found for radial location and the qualitative structure of the mode. The $n = 6$ comparison shows better agreement with experimental data when using the kick model fast ion density profile.

Previously, V&V studies of the linear gyrokinetic simulations of reversed shear Alfvén eigenmodes (RSAEs) excited by fast ions from neutral beam injection (NBI) in the DIII-D tokamak have been carried out [5] by using a gyrokinetic particle code GTC [27], a gyrokinetic continuum code GYRO [28], and a gyro-Landau fluid code TAEFL [21]. Good agreement in RSAE frequency, growth rate, and mode structure have been obtained among these initial value simulations, and between simulation results and experimental measurements using electron cyclotron emission imaging (ECEI) [29]. The successful linear V&V lends some degree of confidence to nonlinear gyrokinetic simulations [30–32] that provide new kinetic insights on nonlinear Alfvén eigenmode dynamics and EP transport, and help the construction of reduced EP transport models [13, 33, 34] which are needed for fast parameter scans, shot-to-shot analysis, and optimization of ITER experiments.

The linear RSAE V&V study presented here expands on the earlier V&V study [5] with a larger sets of simulation codes and with a co-existing TAE when using a more realistic fast ion profile from the kick model. Nevertheless, robust comparisons of theory and experiment would require nonlinear integrated kinetic-MHD simulations, which can investigate the effects of mesoscale Alfvénic instabilities on EP transport as well as nonlinear couplings of Alfvén eigenmodes with microturbulence and MHD instability. To this end, nonlinear verification studies are needed to converge theoretical calculations, and build a reliable computational toolbox to understand EP transport and aid optimizations of ITER experiments.

Acknowledgments

This work is supported by U.S. Department of Energy (DOE) SciDAC project ISEP and AToM, and by DOE grants DE-FG02-07ER54916 and DE-SC0013804 at UCI, DE-AC02-09CH11466 at PPPL, DE-SC0017992, DE-SC0012551, DE-FG02-99ER54531, and DE-FG02-95ER54309 and DE-SC0018108 at GA. This work has been carried out within the framework of the EUROfusion Consortium and has received funding from the Euratom research and training programme 2014–2018 under grant agreement No 633053. This research used resources of the Oak Ridge Leadership Computing Facility at Oak Ridge National Laboratory (DOE Contract No. DE-AC05-00OR22725) and the National Energy Research Scientific Computing Center (DOE Contract No. DE-AC02-05CH11231). The views and opinions expressed herein do not necessarily reflect those of the European Commission. This material is based upon work using the DIII-D National Fusion Facility, a DOE Office of Science user facility, under Awards DE-FC02-04ER54698. DIII-D data shown in this paper can be obtained in digital format by following the links at https://fusion.gat.com/global/D3D_DMP

Disclaimer

This report was prepared as an account of work sponsored by an agency of the United States Government. Neither the United States Government nor any agency thereof, nor any of their employees, makes any warranty, express or implied, or assumes any legal liability or responsibility for the accuracy, completeness, or usefulness of any information, apparatus, product, or process disclosed, or represents that its use would not infringe privately owned rights. Reference herein to any specific commercial product, process, or service by trade name, trademark, manufacturer, or otherwise does not necessarily constitute or imply its endorsement, recommendation, or favoring by the United States Government or any agency thereof. The views and opinions of authors expressed herein do not necessarily state or reflect those of the United States Government or any agency thereof.

Appendix. Simulation models and setups

This section presents a detailed comparison of the simulation models used in each participating code in this study, as well as the simulation set ups used.

A.1. Gyrokinetic model

A.1.1. EUTERPE EUTERPE is three dimensional, full volume, and electromagnetic gyrokinetic particle in cell (PIC) code. It solves the gyrokinetic Vlasov–Maxwell system neglecting $\tilde{B}_{||}$ perturbations. To avoid numerical difficulties

associated with the so-called ‘cancellation problem’, the gyrokinetic equations are formulated using mixed variables [35] and the ‘pullback transformation scheme’ [6]. It can be interpreted as an explicit reset of the time integrator bringing the system back to the v_{\parallel} scheme [36]. The spatial directions are discretized with B-splines (here B-splines of order two have been used). The code uses Fourier filtering of the perturbations in the angular directions. Furthermore, the sparse matrices resulting from the finite element decomposition have been Fourier transformed and filtered to construct a Fourier solver guaranteeing high accuracy. The spatial resolution is provided by using 150 radial and 128 poloidal splines. It is possible to provide a leading Fourier factor ($\sim e^{i(m_p\theta + n_p\phi)}$), which is called ‘phase factor’ in code terminology. It allows to single out the toroidal direction [37] and allows a lower resolution in poloidal direction.

The Vlasov equation is solved using the so-called δf -ansatz [38], i.e. the distribution function is split into an equilibrium part and the perturbation. The number of marker particles is 64 million for the ions, 256 million for the electrons and 64 million for the fast ions. The equilibrium provided by a mapping from the computational domain extends from $r = 0$ to $r = a$ with Dirichlet boundary conditions at the outer boundary and natural boundary conditions for the radial finite elements at the inner. Lost particles are re-inserted such that their weight is zero and the constants of motion are preserved.

Although there are several models of different physical complexities installed in the EUTERPE code, such as fluid electrons and/or ions (FLU-EUTERPE) [39] or perturbative kinetic MHD model (CKA-EUTERPE) [40], here always the full gyrokinetic model with a realistic electron/ion mass ratio is used. The electrons are drift kinetic i.e. their gyro-radius is zero, while for the ion species the gyro-averages resulting from the theory are performed with n_g -point averages where n_g ranges between 4 and 32 and adapts to the size of the gyro-radii [41].

A.1.2. GEM. GEM is a gyrokinetic delta-f PIC code that was originally developed for the study of tokamak core plasma microturbulence and anomalous transport. GEM uses the field-aligned coordinates in general magnetic equilibria. Electromagnetic perturbations are included using the parallel canonical momentum formalism. The split-weight scheme [7, 42] is used to enhance the time step otherwise limited by the fast electron motion along the magnetic field. GEM also has a fluid electron model for studying the long wavelength energetic particle-driven modes [43]. The fluid electron model consists of the electron continuity equation, the isothermal condition for the electron temperature and the Ohm’s law for determining the parallel electric field. Both the kinetic electron model and the fluid electron model are used for the RSAE simulation, and the two models agree. Only the kinetic electron model is used for the TAE simulations. The simulation domain is $0.1 < r/a < 0.9$, with a grid resolution of $(N_x, N_y, N_{\parallel}) = (256, 64, 64)$ in the field-line-following coordinates (x, y, z) , with 16 particles/cell per ion species. The ion FLR effect in particle motion and weight evolution is treated with four-point averaging. The gyrokinetic Poisson

equation is discretized using a full spectral representation of the ion FLR effect in the ion polarization density.

A.1.3. GTC. The gyrokinetic code (GTC) [27, 44] is a full torus particle code using both the δf and full- f methods. Thermal and fast ions are simulated using gyrokinetic equations [45]. The electron drift kinetic equation can be solved either exactly using a conservative scheme for both tearing and non-tearing parity [46], or approximately using a fluid-kinetic hybrid electron model that removes the tearing parity [47]. The perturbed electromagnetic field is solved for from the gyrokinetic Poisson’s equation [48] and Ampère’s Law. GTC has been widely used to study microturbulence [49], Alfvén eigenmodes [50], and other low frequency MHD modes in tokamaks, stellarators [51], and field-reversed configuration [52].

For the present work, marker particles are loaded in velocity space according to a Maxwellian distribution, f_0 , and the plasma perturbation is described via the δf method. The electrons are modeled according to the fluid-kinetic hybrid model [47, 53]. In the lowest order, or adiabatic limit, electrons are described via the fluid continuity equation. In the higher orders, kinetic effects are solved by the particle method for the non-adiabatic part of the electrons distribution using the drift kinetic equation. In this study, we neglect δB_{\parallel} effects [54]. Finite larmor effects are implemented via the four-point average method [55]. The simulation domain used is $\rho = [0.12, 0.9]$, the time step size is $\Delta t = 0.14R_0/v_{A0}$, where v_{A0} and R_0 are the on axis Alfvén speed and major radius, $\Delta r/\rho_i \sim r\Delta\theta/\rho_i \sim 1.7$, where Δr and $r\Delta\theta$ are the radial and poloidal grid spacing, and ρ_i is the local thermal ion gyro-radius. Each particle species has 20 particles per cell.

A.1.4. GYRO. GYRO [28, 56] is a continuum gyrokinetic code with field-aligned coordinates in kinetic phase space: flux-surface label $\hat{r} = \frac{r}{a}$, where r is the flux-surface half width at the centroid height and a is the plasma minor radius; normalized parallel orbit time τ ; pitch angle variable $\lambda = \frac{v_{\perp}^2}{v^2 B}$, where v_{\perp} and v are the perpendicular and total velocities and \hat{B} is the magnetic field normalized to a reference value; and kinetic energy K normalized to the local temperature T : $\hat{E} = \frac{K}{T}$. The toroidal degree of freedom is treated spectrally. The rapid cross-field variation is factored out through a $k_{\parallel} = 0$ eikonal, with the solver finding the slowly-varying envelope function. The slow θ variation of the envelope is neglected in the equations of motion and in the gyro-average. Trapped and passing particles lie on separate phase-space grid points, with τ normalized as is appropriate. The gyrokinetic equations are solved for three kinetic species: electrons, thermal deuterium ions, and hot beam deuterium ions modeled with an equivalent high temperature Maxwellian distribution. Coupling between species occurs through a Poisson–Ampere field solver performed at each time step. The solver considers electrostatic potential ϕ and perpendicular magnetic field fluctuations (through perturbed parallel vector potential A_{\parallel}), but parallel magnetic field fluctuations are neglected in the present study. Both ion species are treated gyrokinetically and

the electrons are treated with drift kinetics. The Eulerian time step uses a hybrid implicit-explicit scheme, with the electron dynamics treated implicitly to avoid tracking stiff electron parallel motion.

The present linear simulations are performed over a radial domain $r = [0.23, 0.83]$ or $\rho = [0.20, 0.81]$, with a grid resolution $(N_r, N_\tau, N_\lambda, N_E) = (150, 20, 8, 8)$ at each value of toroidal mode number n . The λ grid includes four passing and four trapped values. Radial grid points are nonuniformly spaced to optimize resolution of flux surfaces. This gives a mean radial grid spacing of nearly two thermal ion Larmor radii, inadequate for resolving ion-scale drift-wave turbulence but well converged for the presented EP-driven Alfvén eigenmodes. The required time step of $\frac{c_s \Delta t}{a} = 0.01$ is smaller than typical values used for simulating microturbulence due to the faster EP dynamics.

Finite Larmor radius effects are accounted for through a pseudospectral gyro-average of relevant potentials, considering a finite radial stencil around the interest point (20 radial gridpoints here). The stencil is wide enough to adequately treat the largest orbits in the simulation. See [28] for details.

A.1.5. ORB5. ORB5 is a nonlinear gyrokinetic PIC code [8] with extension to electromagnetic physics and multiple species [57–59]. The p_{\parallel} formulation is used and the adjustable control variate method is implemented in ORB5 [57, 60], in order to avoid the ‘cancellation problem’. Recent development in ORB5 allows larger time step size due to the implementation of the ‘pullback transformation scheme’ [6, 35]. The linear, quadratic and cubic splines are implemented in the code for discretization in radial and poloidal directions and the cubic spline is used in this work. The Fourier representation is used in the toroidal direction. Fourier filters are applied in poloidal and toroidal directions in addition to a field-aligned filter which keeps the poloidal harmonics in the range $nq - \Delta m \leq m \leq nq + \Delta m$ and in this work, $\Delta m = 5$ for RSAE simulation and $\Delta m = 16$ for TAE simulation.

The simulation is performed in the radial domain $\rho = [0, 1.0]$, with a grid resolution of $(N_\rho, N_\theta, N_\phi) = (256, 192, 48)$ for RSAE simulations and $(N_\rho, N_\theta, N_\phi) = (256, 256, 64)$ for TAE simulations, where θ and ϕ are poloidal-like and toroidal angles. The number of marker particles is 16 million thermal ions, 64 million for electrons and 16 million fast ions for $n = 4, 5$ RSAEs. Doubled marker numbers are adopted for $n = 3, 6$ RSAEs. Gyro-averages are included for all ion species and the points number for gyro-averaging is determined by using the gyro-adaptive method [41]. The time step size is $dt = 0.065 R_0 / v_{A0}$ (the permissible dt in TAE case is larger), where v_{A0} and R_0 are the on axis Alfvén velocity and major radius. While the traditional δf method and the direct δf method [61] are both implemented in the code, the former one is adopted in the simulation.

A.2. Gyrokinetic-MHD hybrid

A.2.1. MEGA. MEGA is a hybrid simulation code for energetic particles interacting with an MHD fluid [10, 62–64].

The large fast ion pressure profile flattening and the electron temperature fluctuations due to the TAEs observed in a DIII-D experiment were successfully reproduced by comprehensive MEGA simulations [64]. In the MEGA code, the bulk plasma is described by the nonlinear MHD equations, and the energetic particles are simulated with the gyrokinetic PIC method. The electromagnetic field is given by the MHD model. The effects of the energetic particles on the MHD fluid is taken into account through the perpendicular energetic particle current in the MHD momentum equation. Either the full f method or the δf method can be applied to the energetic particles. The thermal ion diamagnetic drift is considered in the MHD momentum equation, and the finite Larmor radius effect is retained for the energetic particle dynamics, using the four-point average method. The spatial derivatives in the MHD equations are calculated with a fourth order finite difference method, and the fourth order Runge–Kutta scheme is employed for the time integration of both the MHD equations and the particle dynamics. For the benchmark results presented in this paper, (128, 16, 256) grids are used for cylindrical coordinates (R, φ, z) , respectively, with $0 \leq \varphi < \pi/2$ for the study of the $n = 4$ RSAE. The number of computational particles is one million.

A.2.2. FAR3D. Gyro-Landau closure techniques [65] allow excitation of Alfvén instabilities within a hybrid (fluid-kinetic) global model; this technique was originally implemented and applied in the TAEFL model [21, 66], and more recently extended to 3D configurations with the FAR3D model [9, 67]. The motivations for such models are: computational efficiency; the fact that the equations can be cast into a matrix eigenmode form, allowing examination of both growing/damped modes, and the capability to follow long-time scale nonlinear phenomena [68]. For the calculations reported here, the FAR3D model was used; this model is based on VMEC equilibria and can treat both 2D and 3D configurations as well as up-down asymmetric tokamaks. The initial equilibrium is obtained from EFIT; this is converted to a VMEC input file and then recalculated using VMEC. The VMEC data are transformed to Boozer coordinates [69], which are the native coordinates used in the code. The version of FAR3D used for this study included two moment equations (density and parallel momentum) for the fast ion component; options are available with three and four moments, which allow extension of the model [22] to non-Maxwellian distribution functions, such as slowing-down distributions. The fast ion moment equations include four scalar closure coefficients [69] that are selected via calibration against analytical results for Alfvén instability growth rates. The MHD component of the FAR3D model is based on the reduced MHD approximation; a poloidal flux evolution equation (Ohm’s law), a toroidal component of the vorticity equation, and a pressure and parallel velocity evolution equation for the thermal plasma (to include sound wave couplings) are included. Toroidal rotation is included, but not used for this paper. Finite Larmor radius effects are introduced into the fast ion equations using Padé approximate fits to the Bessel functions and for the thermal ions using a

perturbative approach. Ion and electron Landau damping is included through perturbative terms in the vorticity equation [70]. Since separate equations for thermal electrons and ions are not currently implemented, an ω^* ion correction is added to the real frequencies of the modes analyzed in this paper. The equations are solved using Fourier series representations for the poloidal and toroidal angle dependencies; the radial variable is the square-root of the normalized toroidal magnetic flux and a finite difference grid is used in this coordinate. The equations can either be integrated in time, using a semi-implicit stepping procedure, or as a single eigenmode solution, based on a targeted Jacobi–Davidson algorithm. For the calculations reported in this paper 400 radial surfaces were used, with 22 to 30 Fourier modes for the perturbed fields and ten Fourier modes for the equilibrium fields. In most of the cases in this paper, the eigensolver option was used instead of the initial value option, since the instabilities studied here had growth rates that were subdominant to other AE and MHD modes.

A.3. Perturbative eigenvalue NOVA simulations

NOVA and NOVA-K codes are linear hybrid MHD/kinetic codes to study EP driven MHD eigenmode instabilities. NOVA solves ideal MHD equations and finds eigenmodes, such as TAEs [11], including such effects as plasma compressibility and realistic geometry. NOVA-K evaluates the wave particle interaction of the eigenmodes of interest such as TAEs or RSAEs by employing the quadratic form with the perturbed distribution function of energetic ions coming from the drift kinetic equations [71]. NOVA-K is able to predict various kinetic growth and damping rates perturbatively, such as the phase space gradient drive from energetic particles, continuum damping, radiative damping, ion/electron Landau damping and trapped electron collisional damping. NOVA is routinely used for AE structure computations and comparisons with the experimentally observed instabilities [29, 72]. The main limitations of the NOVA code are caused by neglecting thermal ion FLR, toroidal rotation, and drift effects in the eigenmode computations. Therefore it can not describe accurately radiative damping for example. Finite element methods are used in radial direction and Fourier harmonics are used in poloidal and toroidal directions. In the results reported here we used the uniform in ψ radial grid with 201 and 256 points in radial and poloidal directions respectively, and poloidal harmonics ranging from 7 to 32.

ORCID iDs

Z.X. Lu  <https://orcid.org/0000-0002-0557-9694>
 D.A. Spong  <https://orcid.org/0000-0003-2370-1873>
 Y. Todo  <https://orcid.org/0000-0001-9323-8285>
 W.W. Heidbrink  <https://orcid.org/0000-0002-6942-8043>
 R.E. Waltz  <https://orcid.org/0000-0002-5203-4830>
 W.L. Zhang  <https://orcid.org/0000-0002-7136-2119>

References

- [1] Pace D.C., Heidbrink W.W. and Van Zeeland M.A. 2015 Keeping fusion plasmas hot *Phys. Today* **68** 34
- [2] Chen L. and Zonca F. 2016 Physics of Alfvén waves and energetic particles in burning plasmas *Rev. Mod. Phys.* **88** 015008
- [3] Collins C. *et al* 2016 Observation of critical-gradient behavior in Alfvén-eigenmode-induced fast-ion transport *Phys. Rev. Lett.* **116** 095001
- [4] Heidbrink W., Collins C., Podestà M., Kramer G., Pace D., Petty C., Stagner L., Van Zeeland M., White R. and Zhu Y. 2017 Fast-ion transport by Alfvén eigenmodes above a critical gradient threshold *Phys. Plasmas* **24** 056109
- [5] Spong D.A., Bass E., Deng W., Heidbrink W., Lin Z., Tobias B., Van Zeeland M., Austin M., Domier C. and Luhmann N.Jr. 2012 Verification and validation of linear gyrokinetic simulation of Alfvén eigenmodes in the DIII-D tokamak *Phys. Plasmas* **19** 082511
- [6] Mishchenko A., Könies A., Kleiber R. and Cole M. 2014 Pullback transformation in gyrokinetic electromagnetic simulations *Phys. Plasmas* **21** 092110
- [7] Chen Y. and Parker S.E. 2003 A δf particle method for gyrokinetic simulations with kinetic electrons and electromagnetic perturbations *J. Comput. Phys.* **189** 463–75
- [8] Jolliet S., Bottino A., Angelino P., Hatzky R., Tran T.-M., McMillan B., Sauter O., Appert K., Idomura Y. and Villard L. 2007 A global collisionless pic code in magnetic coordinates *Comput. Phys. Commun.* **177** 409–25
- [9] Varela J., Spong D. and Garcia L. 2017 Analysis of Alfvén eigenmode destabilization by energetic particles in large helical device using a Landau-closure model *Nucl. Fusion* **57** 046018
- [10] Todo Y. and Sato T. 1998 Linear and nonlinear particle-magnetohydrodynamic simulations of the toroidal Alfvén eigenmode *Phys. Plasmas* **5** 1321–7
- [11] Cheng C.Z. and Chance M.S. 1986 Low- n shear Alfvén spectra in axisymmetric toroidal plasmas *Phys. Fluids* **29** 3695–701
- [12] Lao L., Ferron J., Groebner R., Howl W., John H.S., Strait E. and Taylor T. 1990 Equilibrium analysis of current profiles in tokamaks *Nucl. Fusion* **30** 1035
- [13] Podestà M., Gorelenkova M., Gorelenkov N. and White R. 2017 Computation of Alfvén eigenmode stability and saturation through a reduced fast ion transport model in the transp tokamak transport code *Plasma Phys. Control. Fusion* **59** 095008
- [14] Shi L., Valeo E., Tobias B., Kramer G., Hausammann L., Tang W. and Chen M. 2016 Synthetic diagnostics platform for fusion plasmas *Rev. Sci. Instrum.* **87** 11D303
- [15] Collins C. *et al* 2017 Phase-space dependent critical gradient behavior of fast-ion transport due to Alfvén eigenmodes *Nucl. Fusion* **57** 086005
- [16] Van Zeeland M. *et al* 2016 Electron cyclotron heating can drastically alter reversed shear Alfvén eigenmode activity in DIII-D through finite pressure effects *Nucl. Fusion* **56** 112007
- [17] Podestà M., Gorelenkova M. and White R. 2014 A reduced fast ion transport model for the tokamak transport code transp *Plasma Phys. Control. Fusion* **56** 055003
- [18] Lao L., John H.S., Stambaugh R., Kellman A. and Pfeiffer W. 1985 Reconstruction of current profile parameters and plasma shapes in tokamaks *Nucl. Fusion* **25** 1611
- [19] Hirshman S.P. and Whitson J. 1983 Steepest-descent moment method for three-dimensional magnetohydrodynamic equilibria *Phys. Fluids* **26** 3553–68

- [20] Berk H., Mett R. and Lindberg D. 1993 Arbitrary mode number boundary-layer theory for nonideal toroidal Alfvén modes *Phys. Fluids B* **5** 3969–96
- [21] Spong D., Carreras B. and Hedrick C. 1992 Linearized gyrofluid model of the alpha-destabilized toroidal Alfvén eigenmode with continuum damping effects *Phys. Fluids B* **4** 3316–28
- [22] Spong D.A. 2013 Simulation of Alfvén frequency cascade modes in reversed shear-discharges using a Landau-closure model *Nucl. Fusion* **53** 053008
- [23] Wang Z. *et al* 2013 Radial localization of toroidicity-induced Alfvén eigenmodes *Phys. Rev. Lett.* **111** 145003
- [24] Van Zeeland M. *et al* 2009 Measurements, modelling and electron cyclotron heating modification of Alfvén eigenmode activity in DIII-D *Nucl. Fusion* **49** 065003
- [25] Zonca F., Chen L. and Santoro R.A. 1996 Kinetic theory of low-frequency Alfvén modes in tokamaks *Plasma Phys. Control. Fusion* **38** 2011
- [26] Austin M. and Lohr J. 2003 Electron cyclotron emission radiometer upgrade on the DIII-D tokamak *Rev. Sci. Instrum.* **74** 1457–9
- [27] Lin Z., Hahm T.S., Lee W., Tang W.M. and White R.B. 1998 Turbulent transport reduction by zonal flows: Massively parallel simulations *Science* **281** 1835–7
- [28] Candy J. and Waltz R. 2003 An eulerian gyrokinetic-Maxwell solver *J. Comput. Phys.* **186** 545–81
- [29] Van Zeeland M.A., Kramer G.J., Austin M.E., Boivin R.L., Heidbrin W.W., Makowski M.A., McKee G.R., Nazikian R., Solomon W.M. and Wang G. 2006 Radial structure of Alfvén eigenmodes in the DIII-D tokamak through electron-cyclotron-emission measurements *Phys. Rev. Lett.* **97** 135001
- [30] Bass E. and Waltz R. 2010 Gyrokinetic simulations of mesoscale energetic particle-driven Alfvénic turbulent transport embedded in microturbulence *Phys. Plasmas* **17** 112319
- [31] Zhang H. *et al* 2012 Nonlinear frequency oscillation of Alfvén eigenmodes in fusion plasmas *Phys. Rev. Lett.* **109** 025001
- [32] Chen Y., Munsat T., Parker S., Heidbrink W., Van Zeeland M., Tobias B. and Domier C. 2013 Gyrokinetic simulations of reverse shear Alfvén eigenmodes in DIII-D plasmas *Phys. Plasmas* **20** 012109
- [33] Bass E.M. and Waltz R. 2017 Nonlinear verification of a linear critical gradient model for energetic particle transport by Alfvén eigenmodes *Phys. Plasmas* **24** 122302
- [34] Gorelenkov N.N., Duarte V.N., Podesta M. and Berk H.L. 2018 Resonance broadened quasi-linear (RBQ) model for fast ion distribution relaxation due to Alfvénic eigenmodes *Nucl. Fusion* **58** 082016
- [35] Mishchenko A., Cole M., Kleiber R. and Könies A. 2014 New variables for gyrokinetic electromagnetic simulations *Phys. Plasmas* **21** 052113
- [36] Kleiber R., Hatzky R., Könies A., Mishchenko A. and Sonnendrücker E. 2016 An explicit large time step particle-in-cell scheme for nonlinear gyrokinetic simulations in the electromagnetic regime *Phys. Plasmas* **23** 032501
- [37] Fivaz M., Brunner S., de Ridder G., Sauter O., Tran T., Vaclavik J., Villard L. and Appert K. 1998 Finite element approach to global gyrokinetic particle-in-cell simulations using magnetic coordinates *Comput. Phys. Commun.* **111** 27–47
- [38] Aydemir A.Y. 1994 A unified monte carlo interpretation of particle simulations and applications to non neutral plasmas *Phys. Plasmas* **1** 822–31
- [39] Cole M., Mishchenko A., Könies A., Kleiber R. and Borchardt M. 2014 Fluid electron, gyrokinetic ion simulations of linear internal kink and energetic particle modes *Phys. Plasmas* **21** 072123
- [40] Fehér T.B. 2013 Simulation of the interaction between Alfvén waves and fast particles *PhD Thesis* Universität Greifswald
- [41] Hatzky R., Tran T.M., Könies A., Kleiber R. and Allfrey S.J. 2002 Energy conservation in a nonlinear gyrokinetic particle-in-cell code for ion-temperature-gradient-driven modes in θ -pinch geometry *Phys. Plasmas* **9** 898–912
- [42] Lee W., Lewandowski J., Hahm T. and Lin Z. 2001 Shear-Alfvén waves in gyrokinetic plasmas *Phys. Plasmas* **8** 4435–40
- [43] Chen Y. and Parker S. 2001 A gyrokinetic ion zero electron inertia fluid electron model for turbulence simulations *Phys. Plasmas* **8** 441–6
- [44] Xiao Y., Holod I., Wang Z., Lin Z. and Zhang T. 2015 Gyrokinetic particle simulation of microturbulence for general magnetic geometry and experimental profiles *Phys. Plasmas* **22** 022516
- [45] Brizard A. and Hahm T. 2007 Foundations of nonlinear gyrokinetic theory *Rev. Mod. Phys.* **79** 421
- [46] Bao J., Lin Z. and Lu Z. 2018 A conservative scheme for electromagnetic simulation of magnetized plasmas with kinetic electrons *Phys. Plasmas* **25** 022515
- [47] Deng W., Lin Z. and Holod I. 2012 Gyrokinetic simulation model for kinetic magnetohydrodynamic processes in magnetized plasmas *Nucl. Fusion* **52** 023005
- [48] Lee W. 1987 Gyrokinetic particle simulation model *J. Comput. Phys.* **72** 243–69
- [49] Xie H., Xiao Y. and Lin Z. 2017 New paradigm for turbulent transport across a steep gradient in toroidal plasmas *Phys. Rev. Lett.* **118** 095001
- [50] Liu Y., Lin Z., Zhang H. and Zhang W. 2017 Excitation of low frequency Alfvén eigenmodes in toroidal plasmas *Nucl. Fusion* **57** 114001
- [51] Spong D.A., Holod I., Todo Y. and Osakabe M. 2017 Global linear gyrokinetic simulation of energetic particle-driven instabilities in the lhd stellarator *Nucl. Fusion* **57** 086018
- [52] Schmitz L. *et al* 2016 Suppressed ion-scale turbulence in a hot high- β plasma *Nat. Commun.* **7** 13860
- [53] Holod I., Zhang W., Xiao Y. and Lin Z. 2009 Electromagnetic formulation of global gyrokinetic particle simulation in toroidal geometry *Phys. Plasmas* **16** 122307
- [54] Dong G., Bao J., Bhattacharjee A., Brizard A., Lin Z. and Porazik P. 2017 Gyrokinetic particle simulations of the effects of compressional magnetic perturbations on drift-Alfvénic instabilities in tokamaks *Phys. Plasmas* **24** 081205
- [55] Lee W. 1983 Gyrokinetic approach in particle simulation *Phys. Fluids* **26** 556–62
- [56] Candy J. and Waltz R.E. 2003 Anomalous transport scaling in the DIII-D tokamak matched by supercomputer simulation *Phys. Rev. Lett.* **91** 045001
- [57] Bottino A., Vernay T., Scott B., Brunner S., Hatzky R., Jolliet S., McMillan B., Tran T.-M. and Villard L. 2011 Global simulations of tokamak microturbulence: finite- β effects and collisions *Plasma Phys. Control. Fusion* **53** 124027
- [58] Bottino A. and Sonnendrücker E. 2015 Monte carlo particle-in-cell methods for the simulation of the Vlasov–Maxwell gyrokinetic equations *J. Plasma Phys.* **81** 435810501
- [59] Biancalani A., Bottino A., Cole M., Di Troia C., Lauber P., Mishchenko A., Scott B. and Zonca F. 2017 Nonlinear interplay of Alfvén instabilities and energetic particles in tokamaks *Plasma Phys. Control. Fusion* **59** 054004
- [60] Hatzky R., Könies A. and Mishchenko A. 2007 Electromagnetic gyrokinetic pic simulation with an adjustable control variates method *J. Comput. Phys.* **225** 568–90
- [61] Allfrey S.J. and Hatzky R. 2003 A revised δf algorithm for nonlinear pic simulation *Comput. Phys. Commun.* **154** 98–104

- [62] Todo Y. 2006 Properties of energetic-particle continuum modes destabilized by energetic ions with beam-like velocity distributions *Phys. Plasmas* **13** 082503
- [63] Todo Y., Van Zeeland M.A., Bierwage A. and Heidbrink W. 2014 Multi-phase simulation of fast ion profile flattening due to Alfvén eigenmodes in a DIII-D experiment *Nucl. Fusion* **54** 104012
- [64] Todo Y., Van Zeeland M.A., Bierwage A., Heidbrink W. and Austin M. 2015 Validation of comprehensive magnetohydrodynamic hybrid simulations for Alfvén eigenmode induced energetic particle transport in DIII-D plasmas *Nucl. Fusion* **55** 073020
- [65] Hammett G.W. and Perkins F.W. 1990 Fluid moment models for Landau damping with application to the ion-temperature-gradient instability *Phys. Rev. Lett.* **64** 3019
- [66] Spong D., Carreras B. and Hedrick C. 1994 Nonlinear evolution of the toroidal Alfvén instability using a gyrofluid model *Phys. Plasmas* **1** 1503–10
- [67] Varela J., Spong D. and Garcia L. 2017 Analysis of Alfvén eigenmodes destabilization by energetic particles in TJ-II using a Landau-closure model *Nucl. Fusion* **57** 126019
- [68] Spong D.A. 2014 Long-term Landau-fluid simulation of Alfvén eigenmode instabilities *Plasma Fusion Res.* **9** 3403077
- [69] Boozer A.H. 1981 Establishment of magnetic coordinates for a given magnetic field *Technical Report* Plasma Physics Lab., Princeton Univ., NJ, USA
- [70] Hedrick C., Leboeuf J.-N. and Spong D. 1992 Alpha-Alfvén local dispersion relation and solutions *Phys. Fluids B* **4** 3869–82
- [71] Cheng C.Z. 1992 Kinetic extensions of magnetohydrodynamics for axisymmetric toroidal plasmas *Phys. Rep.* **211** 1–51
- [72] Kramer G.J. 2006 Interpretation of core localized Alfvén eigenmodes in DIII-D and joining european torus reversed magnetic shear plasmas *Phys. Plasmas* **13** 056104